Study of the flow field past dimpled aerodynamic surfaces: numerical simulation and experimental verification

IOP Conf. Series: Journal of Physics: Conf. Series **923** (2017) 012030 doi:10.1088/1742-6596/923/1/012030

Study of the flow field past dimpled aerodynamic surfaces: numerical simulation and experimental verification

L Binci[1], G Clementi[1], V D'Alessandro[1], S Montelpare[2] and R Ricci[1]

[1] Dipartimento di Ingegneria Industriale e Scienze Matematiche
Università Politecnica delle Marche
Via Brecce Bianche, 60100 Ancona (AN), Italy
[2] Dipartimento di Ingegneria e Geologia
Università degli Studi "G. D'Annuzio" di Chieti–Pescara
Viale Pindaro 42, 65127, Pescara (PE), Italy

E-mail: l.binci@univpm.it

Abstract. This work presents the study of the flow field past of dimpled laminar airfoil. Fluid dynamic behaviour of these elements has been not still deeply studied in the scientific community. Therefore Computational Fluid-Dynamics (CFD) is here used to analyze the flow field induced by dimples on the NACA 64-014A laminar airfoil at Re $= 1.75 \cdot 10^5$ at $\alpha = 0°$. Reynolds Averaged Navier–Stokes (RANS) equations and Large-Eddy Simulations (LES) were compared with wind tunnel measurements in order to evaluate their effectiveness in the modeling this kind of flow field. LES equations were solved using a specifically developed OpenFOAM solver adopting an L–stable Singly Diagonally Implicit Runge–Kutta (SDIRK) technique with an iterated PISO-like procedure for handling pressure-velocity coupling within each RK stage. Dynamic Smagorinsky subgrid model was employed. LES results provided good agreement with experimental data, while RANS equations closed with k–ω–γ–$\widetilde{\mathrm{Re}_{\theta,\mathrm{t}}}$ approach overstimates laminar separation bubble (LSB) extension of dimpled and un–dimpled configurations. Moreover, through skin friction coefficient analysis, we found a different representation of the turbulent zone between the numerical models; indeed, with RANS model LSB seems to be divided in two different parts, meanwhile LES model shows a LSB global reduction.

1. Introduction

In the recent years the increasing interest of governments to diversification of electrical production source is realized with renewable sources plant installation increase. The wind power sector is one of the most developed, thanks also to the innovative construction techniques that have led to wind turbines size growth and a consequent electricity production optimization [1]. It is clear that the development of high efficiency blades still plays a central role in the design of new generation wind turbine. Laminar airfoils can satisfy thees requirements: indeed thees airfoils operate for a certain angles of attack without increasing their aerodynamic drag. However, such airfoils are often affected by a laminar separation bubble (LSB) which produces a reduction of the aerodynamic performance. It is worth nothing that the adoption of dimples to reduce the drag is credible since the accidental discovery of drag reduction by surface roughening on

golf balls. Nevertheless many papers have been devoted to study dimples behavior for bluff body flows and heat transfer enhancement in internal flows; we can not find in the present literature any study that addresses the dimples effect on aerodynamic surfaces for transitional flows. However few researches provide some information about flow structure due to dimples on a channel surface and the influence of dimple depths, [2, 3]. Moreover Lake, [4], in his PhD thesis, conducted experimental tests on a gas turbine blade cascade in order to estimate the best shape and position of the dimples elements. So the main aim of this research is to deeply investigate the dimples effect on aerodynamic surfaces. In particular our efforts have been oriented on low Reynolds number operating airfoils which are of interest for wind energy applications. In particular the impact of dimples on the reduction of LSB was faced. Therefore the flow field past a dimpled NACA 64–014A laminar airfoil was carefully studied. This airfoil was selected because its abrupt pressure recovery and the systematic presence of a LSB. Hence this element allows to evaluate dimples performance about the LSB reduction. The airfoil was studied at $\alpha = 0°$ and $\mathrm{Re} = 1.75 \cdot 10^5$: the dimpled configuration consists in one row of these elements placed at 55 % of chord length with one dimple diameter spacing in the span-wise direction. Firstable Reynolds Averaged Navier–Stokes (RANS) solution were obtained using the well–known commercial CFD code `Star-CCM+`. On the other hand, Large-Eddy Simulations (LES) were performed in order to investigate the flow mechanism in the dimple zone and to reconstruct the flow features in the downstream region. LSB modeling is well recognized challenging task in the CFD community and in the present literature we can find several paper addressing this topic, [5, 6, 7, 8]; however, in the authors knowledge we cannot find any detailed study about LSB reduction modeling using dimples, hence this element can be considered a point of novelty of this paper. Our numerical investigations were validated using experimental data obtained at Environmental Wind Tunnel of the "Università Politecnica delle Marche". The results, presented in this paper, show that dimpled NACA 64-014A airfoil, compared with its un–dimpled version, experiences a LSB reduction.

The paper is organized as follows. Sec. 2 presents the dimples geometric configuration. Sec. 3 briefly describes the flow models and the discretization techniques adopted for their solution. Sec. 4 treats the description of the experimental set–up. Sec. 5 is devoted to the results and Sec. 6 contains the conclusions.

2. Dimple geometric configuration

The dimples geometric features are reported in Fig.1 (values expressed in chord length percent, % c): a spherical cut of 4.7% c as executive diameter and 0.705% c in depth make an elliptic dimple, depending of airfoil local curvature. The dimple axis is placed at 55% c and it is perpendicular to airfoil surface, thus we have a 3.35% c equivalent diameter (ratio between perimeter and π), as reported in Table 1. The dimpled airfoil has only one row of these elements with about one dimple diameter spacing in the spanwise direction.

Table 1. Dimpled NACA 64-014A geometric details; values expressed in chord length percent

x_D	D_{exec}	h	D^*	$\frac{h}{D^*}$
55	4.7	0.705	3.35	0.2107

3. Numerical modeling

For the numerical simulations, RANS and LES approaches were used. For un–dimpled airfoil a RANS 2D model was used, while 3D domain with 14% c spanwise depth is used for dimpled configuration (consisting of two consecutive dimples representation) and LES un–dimpled case.

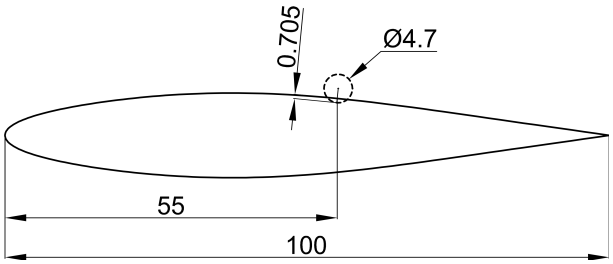

Figure 1. Dimples geometric configuration

A C–shaped domain with hexaedral elements was built. The employed grid has a viscous sublayer scaled first cell height, y^+, of approximately 1. The value of y^+ is estimated as $y^+ = \frac{u_\tau}{\nu} y_c$, where $u_\tau = \sqrt{\tau_w/\rho}$ is the friction velocity, τ_w is the viscous stress component measured at the wall, and y_c is the height of the cells next to the wall which was fixed equal to 10^{-4} c.
The starting 2D domain consists of $1.75 \cdot 10^5$ quadrilateral elements. We have to note that 290 cells were used to discretized the airfoil along the chord length, 180 cells were adopted in the wake region, while 195 in the direction normal to the airfoil. The 3D domain, used for LES computations, was obtained extruding the 2D one in the spanwise direction using 40, uniformly spaced, cells. Thus the total cells' number was $5.6 \cdot 10^6$. The dimples curvature strictly requires a local mesh refinement, thus nodes' number was increased from 290 to 345 for the chord direction and from 40 to 112 for the spanwise direction. In particular the dimples were discretized using 44 elements along its diameter. The obtained computational grid owns $22.1 \cdot 10^6$ cells. Moreover a coarse mesh, having $3.1 \cdot 10^6$ of cells, was also carried out by halving the cells' number in all the x–y–z direction. Fine and coarse computational grids for the dimpled configuration are showed in Fig.2.

For RANS simulations, laminar–to–turbulent transition model available within the commercial CFD software `Star-CCM+` was used. In particular k-ω SST model with γ-$\widetilde{\mathrm{Re}_{\theta,\mathrm{t}}}$ transitional approach was chosen. Unfortunately, only first order upwind scheme can be used for convective terms discretization in this solver. In order to overcome the dissipation induced by the flow model and numerics the free–stream turbulent intensity was set about 3 times greater than turbulent intensity of the experimental tests.
LES seeks to calculate the large energetic structures in a turbulent flow and it allows to reduce the computational resources required by DNS. The LES approach filters the Navier–Stokes equations and it inserts a closure approximation for unresolved turbulent structures. Such models are based on the decomposition of the fluid–dynamic quantities in resolved and unresolved components, $[\overline{\mathbf{u}}, \overline{p}]$ and $[\mathbf{u}', p']$, respectively, so that $\mathbf{u} = \overline{\mathbf{u}} + \mathbf{u}'$ and $p = \overline{p} + p'$ [9]. In order to derive a set of equations for $\overline{\mathbf{u}}$ and $\overline{p}$, a filtering procedure is performed over the Navier–Stokes. Filtered equations reads

$$\begin{aligned} &\boldsymbol{\nabla} \cdot \overline{\mathbf{u}} = 0 \\ &\frac{\partial \overline{\mathbf{u}}}{\partial t} + \boldsymbol{\nabla} \cdot (\overline{\mathbf{u}} \otimes \overline{\mathbf{u}}) = -\frac{1}{\rho} \boldsymbol{\nabla} \bar{p} + \boldsymbol{\nabla} \cdot (\nu \boldsymbol{\nabla} \overline{\mathbf{u}}) - \boldsymbol{\nabla} \cdot \mathbf{B} \end{aligned} \tag{1}$$

where $\mathbf{B} = \overline{\mathbf{u} \otimes \mathbf{u}} - \overline{\mathbf{u}} \otimes \overline{\mathbf{u}}$ is the so called subgrid–scale stress tensor; $\mathbf{B}$ model is the effect of the unresolved scales on the resolved one, [10].
Usually the $\mathbf{B}$ tensor is modeled in analogy with Boussinesque approximation by introducing a subgrid–scale viscosity, ν_{sgs}, as follows:

$$-\mathbf{B} + \frac{2}{3} k_{sgs} \mathbf{I} = \nu_{sgs} \left(\boldsymbol{\nabla} \overline{\mathbf{u}} + \boldsymbol{\nabla} \overline{\mathbf{u}}^T \right) \tag{2}$$

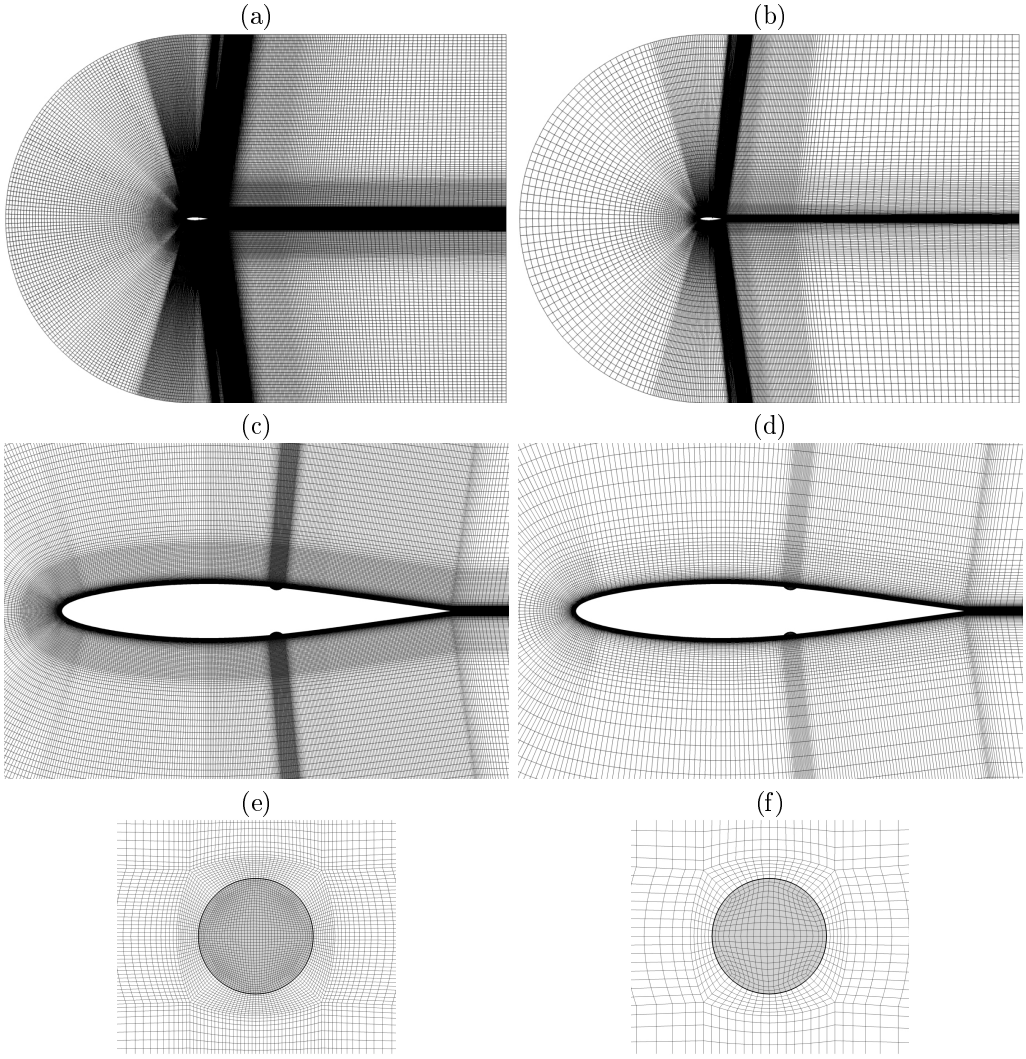

Figure 2. Comparison between fine grid (a,c,e) and coarse grid (b,d,f)

where k_{sgs} is sub–grid kinetic energy and $\mathbf{I}$ the identity tensor. Replacing $\mathbf{B}$ from eq. 2 in eq. 1, we obtain the LES governing equations:

$$\begin{aligned} &\boldsymbol{\nabla} \cdot \overline{\mathbf{u}} = 0 \\ &\frac{\partial \overline{\mathbf{u}}}{\partial t} + \boldsymbol{\nabla} \cdot (\overline{\mathbf{u}} \otimes \overline{\mathbf{u}}) = -\boldsymbol{\nabla} \bar{P} + \boldsymbol{\nabla} \cdot \left[(\nu + \nu_{sgs}) \left(\boldsymbol{\nabla} \overline{\mathbf{u}} + \boldsymbol{\nabla} \overline{\mathbf{u}}^T \right) \right] \end{aligned} \tag{3}$$

with $\bar{P} = \frac{2}{3} k_{sgs} + \bar{p}/\rho$. The sub–grid scales models based on eq. 2 produce the mean (in the statistical sense) dissipation provided by the unresolved eddies. In particular, in this work we have considered dynamic version, [11, 12] of the Smagorinksy subgrid scale model, [10]. Therefore a specifically developed `OpenFOAM` solver named `dirkFoam` has been adopted to solve the flow governing equations. `OpenFOAM` (Open-source Field Operation and Manipulation) code [13] is unstructured finite volume solver released under the GNU Public License (GPL). The code's object-oriented structure enables users to implement their own models and solvers in the baseline codes with relatively little effort (see for example [14, 15, 16]).
The adopted solver has been developed by our group for DNS/LES applications in order to guarantee very low dissipation in time integration, [17, 18]. It adopts a third–order accurate

Singly Diagonally Runge–Kutta (SDIRK) scheme for time integration and for each implicit Runge–Kutta stage, a PISO–like procedure based on Rhie–Chow correction, [19], in the spirit of OpenFOAM PISO implementation is employed, [17, 18]. Moreover all diffusive terms and pressure gradients were approximated with a second–order accuracy, while the convective terms were discretized using high–resolution NVD Gamma scheme, [20]. For what concerns linear solvers, we used a preconditioned bi–conjugate gradient method (PBiCG) with a diagonal incomplete–LU (asymmetric) preconditioner for the momentum equation. For the pressure, on the other hand, we used a preconditioned conjugate gradient method (PCG) with a diagonal incomplete Cholesky preconditioner. The linear system for pressure was solved using a local accuracy of 10^{-6}, whereas the other systems were considered converged when the residuals reached 10^{-9}.Lastly we want also to remark that no wall functions were used, standard inflow/outflow boundary conditions were adopted and the flow periodicity was assumed to be in the span–wise direction.
The computations involving the largest number of grid cells were completed on the GALILEO supercomputing facility at CINECA using 384 CPU–cores. The solutions on the coarser grids were obtained on a small Linux Cluster with 6 AMD Opteron-based nodes for a total of 96 CPU cores operating at 2.6 GHz.

4. Experimental apparatus

Figure 3. (Left) Wing model in EWT of Università Politecnica delle Marche. (Right) Angle of attack rotation system

The experiments were performed at the Environmental Wind Tunnel (EWT) of the "Università Politecnica delle Marche". The EWT test chamber consists of three main sections: the first is used for aerodynamic tests requiring a uniform velocity distribution and a low turbulence level; the second is used to test reciprocal interference effects between slender bodies; the latter is used to test wind effects over buildings, structures, orography models which are subjected to fully developed environmental boundary layers. The wind tunnel is supplied by a fan having a constant rotational speed of 975 RPM, consisting of 16 blades with an adjustable pitch that ensure a regulated wind velocity in the test section between 5 m/s and 40 m/s. Constant Temperature Hot Wire Anemometer (CTA HWA) measurements showed a lack of flow uniformity less than 2.5% and a turbulence intensity level less than 0.3% on an area larger than 90% of the test cross section. Velocity and turbulence measurements are obtained with Dantec CTA

system equipped with a pneumatic calibration unit. The wind tunnel is also equipped with a compact heat exchanger able to control temperature variations inside a range of one Celsius degree. NACA 64-014A dimpled and un–dimpled airfoils are tested. The wing models have

Figure 4. (a) Wing model modules. (b) Pressure holes

a chord and span of 0.45 m and 1.4 m respectively. They are formed by three modules: two modules of wooden template and balsa wood cover and one module formed by tho half birch plywood wooden shells. Pressure measurements were obtained by means of a Games 5266 very low range differential pressure transducer (±50 Pa operating range) with a typical error below 1% FS BSL. To obtain the airfoil pressure coefficient distribution, this device in sequentially connected to all the pressure taps drilled in the section of the wings. The pressure holes are placed along the wooden shells airfoil section as showed in Fig.4. The original airfoil has one row of pressure taps, while the dimpled one has a row passing through the middle section of a dimple and a row between two consecutive dimples. The models are constrained to the wind tunnel by means of a specific framework in order to avoid mechanical vibrations transmission. The angle of attack is set by means of a zero–backlash cycloidal gear train with a graduated indicator and a Handel, see Fig.3.

5. Results

This section presents a comparison of the pressure distribution as well as drag coefficient obtained from LES and RANS computations of the dimpled and un–dimpled airfoil. Finally computed pressure distributions are compared with experimental data.
In Fig. 5 we show a representation of the vortex structures computed using LES technique and identified using the Q–criterion; it is very easy to note as coarse grid results exhibits a loss in the vortical structures resolution.

5.1. Differences between LES and RANS model

As can be seen in Fig. 6, C_p distributions show that our numerical solutions predict a more abrupt pressure recovery for the un–dimpled airfoil configuration. However RANS and LES approaches provide different results downstream the dimples region in terms of LSB modification. Indeed, as shown in Fig. 7, RANS model produces a sort of splitting of the LSB around the half dimple section, meanwhile LES solution indicates a LSB length global reduction (over 13.6% c), with a restricted attached flow area downstream the dimples.

Furthermore, we have to note that the grid resolution is more significant for the LES approach than for the RANS one, in particular coarse grid overestimates the dimples effect and underestimates C_f value on turbulent reattachment area, as can be seen in Fig. 8(a).

Lastly, Table 2 reports the impact of the different turbulence models here used on the LSB extension prediction. Differently Table 3 shows the computed drag coefficients. In particular, we can note that RANS cases and coarse grid LES solution provide a similar global C_D reduction if compared to un–dimpled configuration. On the other hand, LES model with finer grid provides

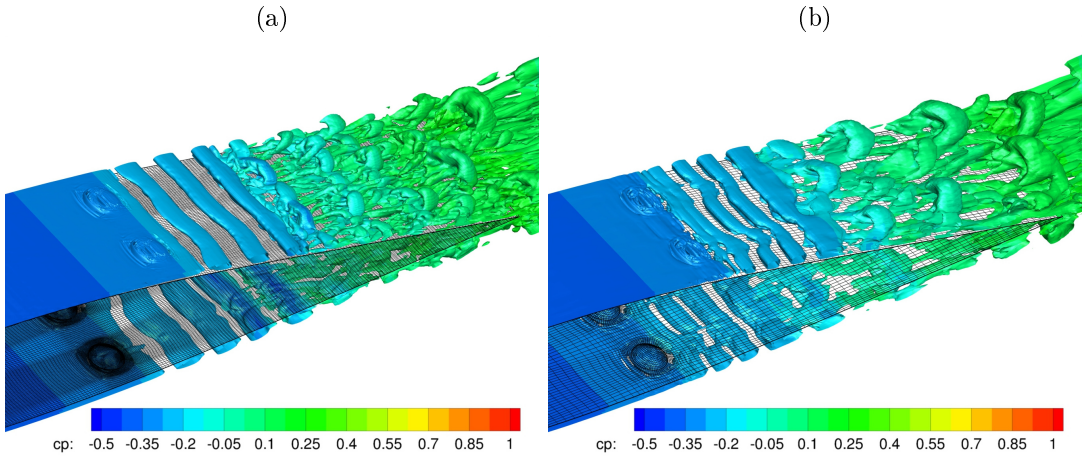

Figure 5. Vortical structures, identified by the Q-criterion ($Q = 0.5u_\infty^2/c^2$), isosurfaces colored by pressure coefficient; (a) fine mesh, (b) coarse mesh.

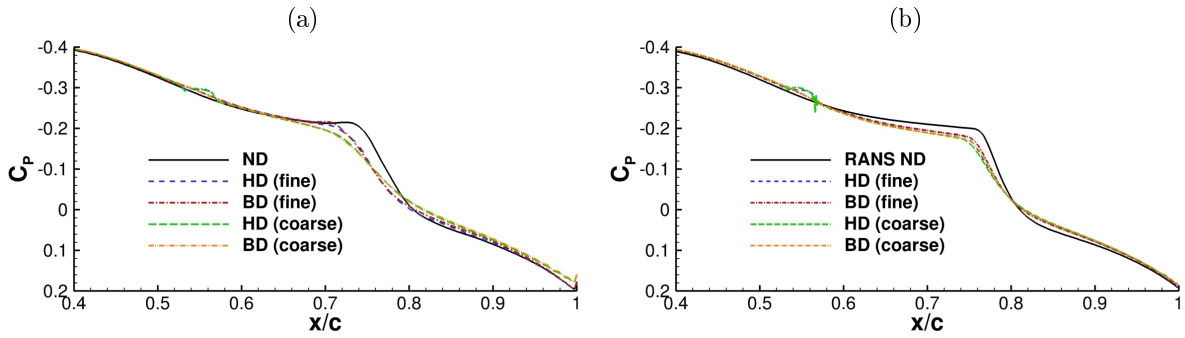

Figure 6. C_p distribution; (a) LES model, (b) RANS model

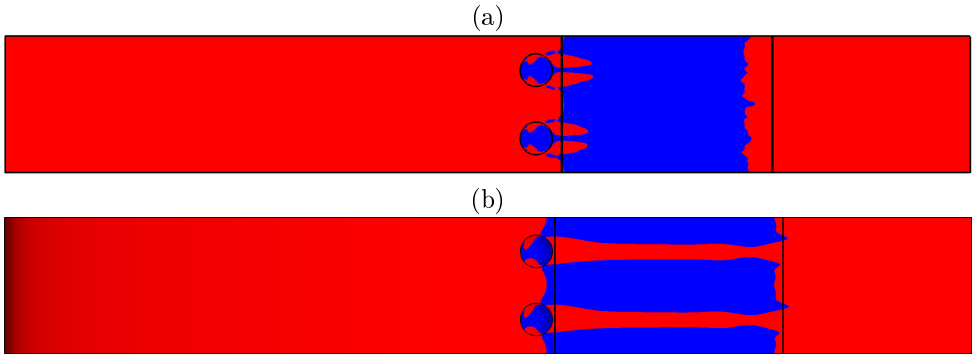

Figure 7. Visualization of positive and negative C_f zones, in red and blue respectively; (a) LES model, (b) RANS model. Blue zones represent the LSB extension of the dimpled airfoil cases, while the vertical black lines indicate the starting-ending flow separation points of the un–dimpled ones.

a minor C_D reduction due to a shear drag increase. Anyway, drag coefficients obtained by RANS model are higher than the LES ones.

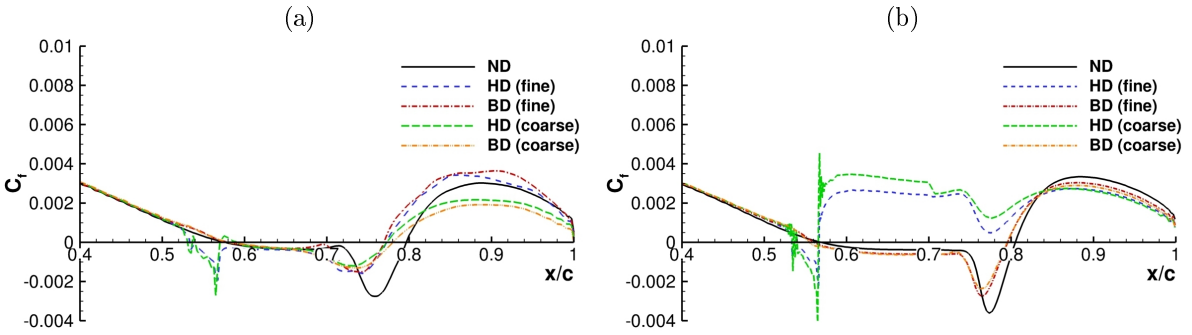

Figure 8. C_f distribution; (a) LES model, (b) RANS model

Table 2. LSB extension; separation and reattachment points expressed in chord length percent. ND = no dimpled airfoil section, HD = half dimple airfoil section, BD = between dimples section.

Section	LES		RANS	
	x_s/c	x_r/c	x_s/c	x_r/c
ND	57.6	79.6	56.9	80.5
HD	53.3	77.4	–	–
BD	58.0	77.0	56.0	79.5

Table 3. Comparison of drag coefficients. C_D = total drag coefficient, $C_{D,p}$ = pressure drag coefficient, $C_{D,f}$ = friction drag coefficient

	$C_D \cdot 10^2$	$C_{D,p} \cdot 10^2$	$C_{D,f} \cdot 10^2$	ΔC_D [%]
LES no dimple	1.188	0.524	0.664	
LES dimple fine grid	1.181	0.465	0.716	-0.59
LES dimple coarse grid	1.155	0.495	0.660	-2.81
RANS no dimple	1.228	0.561	0.667	
RANS dimple fine grid	1.193	0.512	0.681	-2.82
RANS dimple coarse grid	1.192	0.505	0.687	-2.93

5.2. Comparison with experimental data

The pressure coefficient, C_p, distributions of the original and dimpled airfoil are depicted in Fig. 9. Both LES and RANS simulations are in good agreement with experimental data up to 55% c, *i.e.* in the fully laminar zone. In the laminar separation region, the predicted pressure coefficients are not in agreement; however their differences fall inside the experimental uncertainty. Differently in laminar–to–turbulent transition region, as well as in turbulent reattachment one, LES results put in evidence a better fitting with the experimental data if compared with RANS solutions. In particular RANS results are not in good agreement with experiments. As showed in Fig. 10, our dimpled and un–dimpled configurations put in evidence a similar behaviour of the adopted numerical models.

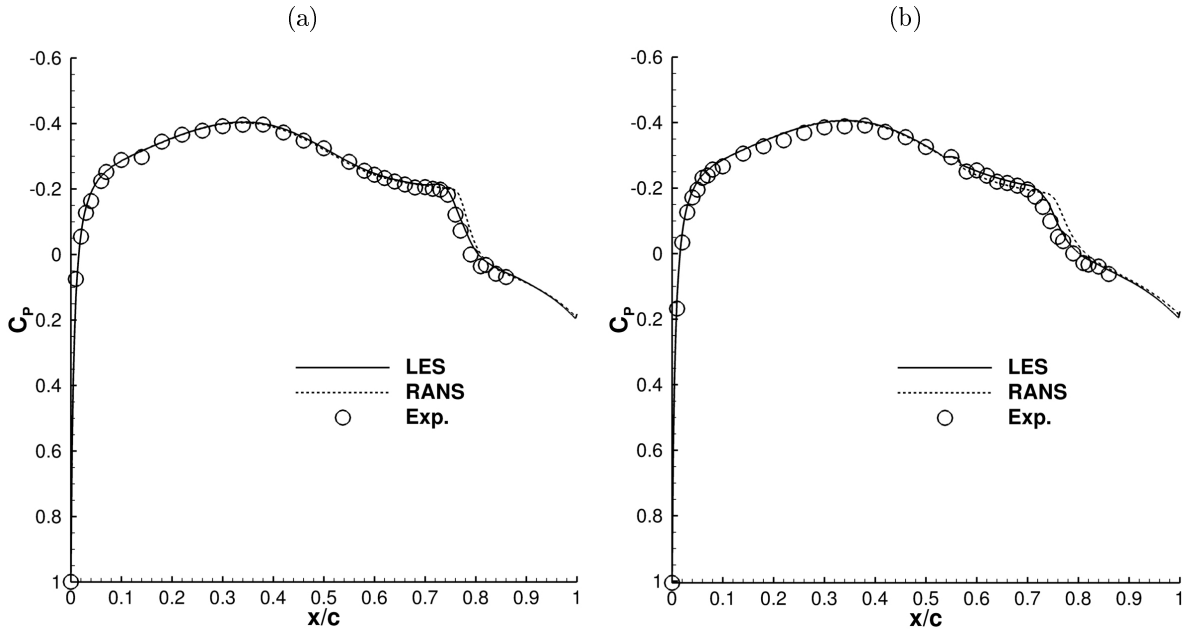

Figure 9. Comparison of C_p with experimental data; (a) un–dimpled airfoil, (b) dimpled airfoil

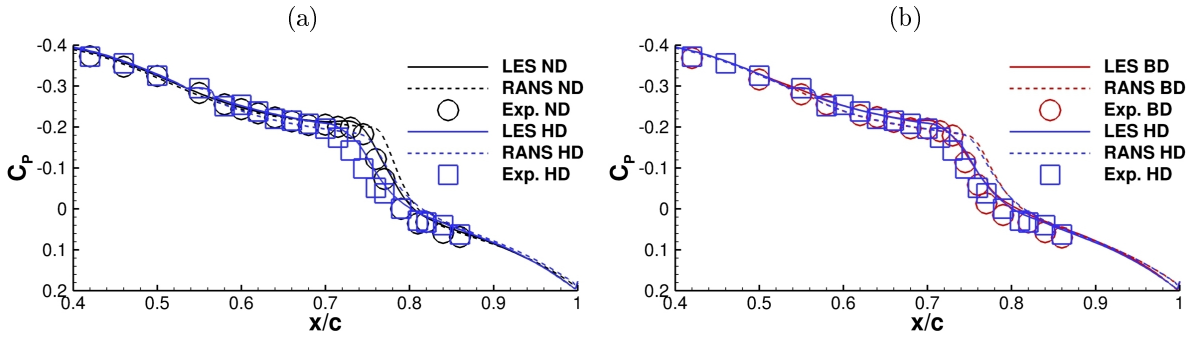

Figure 10. C_p distributions; (a) Comparison of original and dimpled airfoil; (b) differences between the two dimpled airfoil sections. For symbols see caption of table 2

6. Conclusion

In this paper, dimples effect on NACA 64-014A airfoil at Re $= 1.75 \cdot 10^5$ and $\alpha = 0°$ was presented. In particular, the dimples impact on the reduction of the LSB is faced. Therefore, RANS simulations, within a commercial solver, and LES simulations, with a low-dissipative algorithm developed by our group, were used. For LES computations, dynamic version of the Smagorinksy subgrid scale model were used. An experimental measurement were also carried out for validation purposes.

It has been shown that dimples application produces a reduction of the LSB extension. RANS model overestimates the laminar–to–turbulent transition and turbulent reattachment locations of the dimpled and un–dimpled airfoils,while LES model provides better agreement with experimental data for both the cases. Therefore, LES is able to capture the main features of the flow past the dimpled and un–dimpled airfoils. The main drawback of the LES approach is related to its high computational costs and, for this reason, the presented analysis is limited only to a single angle of attack.

In conclusion, dimples application on NACA 64-014A airfoil at Re $= 1.75 \cdot 10^5$ and $\alpha = 0°$

produces a reduction of the LSB extension and a consequent pressure drag decrease. Both numerical models show a total drag reduction, while experimental force measurements are still in processing, with a preliminary good agreement. This is very intresting because dimple application could be the way to reduce the drag by preserving the general blade features of a wind turbine. Indeed, a drag reduction without any lift change will have the double benefit of an increased tangential force and a reduced axial force, i.e. an electric power production increase and a minor mechanical stress for a wind turbine. Future work will be devoted to the evaluation of both the angle of attack and the Re number effects.

7. Acknowledgements

We acknowledge the CINECA Award N. HP10CDBABZ YEAR 2016 under the ISCRA initiative, for providing high-performance computing resources and support.

References

[1] Yu-Fong Huang Xing-Jia Gan P T C 2017 *Renew Energ* **102** 98–106
[2] Ligrani P M, Harrison J L, Mahmmod G I and Hill M L 2001 *Phys Fluids* **13(11)**
[3] Won S Y and Ligrani P M 2007 *Mechl Sci Technol* **21**
[4] Lake J 1999 *Flow Separation Prevention on a Turbine Blade in Cascade at Low Reynolds Number* Ph.D. thesis Air Force Institute of Technology, Ohio
[5] Lee D, Nonomura T, Oyama A and Fujii K 2017 *Int J Comp Fl Dyn* **31** 57–67
[6] Catalano P, Mele B and Tognaccini R 2015 *Comput Fluids* **109** 67–71
[7] Crivellini A and D'Alessandro V 2014 *Int J Heat Fluid Fl* **47** 70–83
[8] Crivellini A, D'Alessandro V, Di Benedetto D, Montelpare S and Ricci R 2014 *J Phys: Conf Ser* **501**
[9] Rogallo R and Moin P 1984 *Annu Rev Fluid Mech* **16** 99–137
[10] Smagorinsky J 1963 *Mon Weather Rev* **91** 99–164
[11] Germano M, Piomelli U, Moin P and Cabot W 1991 *Physics of Fluids* **3** 1760–1765
[12] Lilly D 1991 *Phys Fluids* **4** 633–635
[13] Weller H, Tabor G, Jasak H and Fureby C 1998 *Comput Phys* **12** 620–631
[14] D'Alessandro V, Montelpare S and Ricci R 2016 *Comput Fluids* **136** 152–156
[15] D'Alessandro V, Montelpare S, Ricci R and Zoppi A 2017 *Energy* **130** 402 – 419
[16] Silva L and Lage P 2011 *Comput Chem Eng* **35** 2653–2666
[17] D'Alessandro V, Binci L, Montelpare S and Ricci R 2017 *Comput Phys Commun*
[18] D'Alessandro V, Zoppi A, Binci L and Ricci R 2016 *Int J Comp Meth Exp Meas* **4(4)** 594–603
[19] Ferziger J and Peric M 1999 *Computational Methods for Fluid Dynamics* (Springer)
[20] Jasak H, Weller H and Gosman A 1999 *Intl J Num Meth Fl* **31** 431–449